

# Improved performance and stability in quantum dot solar cells through band alignment engineering

Chia-Hao M. Chuang<sup>1</sup>, Patrick R. Brown<sup>2</sup>, Vladimir Bulović<sup>3</sup> and Mounji G. Bawendi<sup>4\*</sup>

**Solution processing is a promising route for the realization of low-cost, large-area, flexible and lightweight photovoltaic devices with short energy payback time and high specific power. However, solar cells based on solution-processed organic, inorganic and hybrid materials reported thus far generally suffer from poor air stability, require an inert-atmosphere processing environment or necessitate high-temperature processing<sup>1</sup>, all of which increase manufacturing complexities and costs. Simultaneously fulfilling the goals of high efficiency, low-temperature fabrication conditions and good atmospheric stability remains a major technical challenge, which may be addressed, as we demonstrate here, with the development of room-temperature solution-processed ZnO/PbS quantum dot solar cells. By engineering the band alignment of the quantum dot layers through the use of different ligand treatments, a certified efficiency of 8.55% has been reached. Furthermore, the performance of unencapsulated devices remains unchanged for over 150 days of storage in air. This material system introduces a new approach towards the goal of high-performance air-stable solar cells compatible with simple solution processes and deposition on flexible substrates.**

Near-infrared PbS quantum dots (QDs) composed of earth-abundant elements<sup>2</sup> have emerged as promising candidates for photovoltaic applications because of a tunable energy bandgap that covers the optimal bandgap range for single and multi-junction solar cells<sup>1</sup>. The QD surface ligands<sup>3–7</sup> and the photovoltaic device architecture<sup>8–17</sup> play crucial roles in determining the optoelectronic properties of QD solar cells. Advances in QD surface passivation, particularly through the use of halide ions as inorganic ligands<sup>4</sup>, have led to rapid improvements in QD solar cell power conversion efficiencies to 7%<sup>5,15,16</sup> as a result of a lower density of trapped carriers than in their organic ligands counterparts<sup>4</sup>. Furthermore, recent studies have demonstrated the ability to control the band edge energies of QD films through ligand exchange<sup>18–20</sup>. However, fabrication of these recent QD devices requires high-temperature annealing (>500 °C) of the TiO<sub>2</sub> window layer<sup>5,16</sup> or two different processing atmospheres, including an inert gas environment<sup>15</sup>. Although good stability has been claimed, the devices still show performance degradation to ~85% of their original efficiencies within one week, even under inert atmosphere<sup>5,16</sup>. Here, we demonstrate ZnO/PbS solar cells in which the PbS QD and ZnO nanocrystals are both solution-processed in air and at room temperature. We demonstrate a device architecture

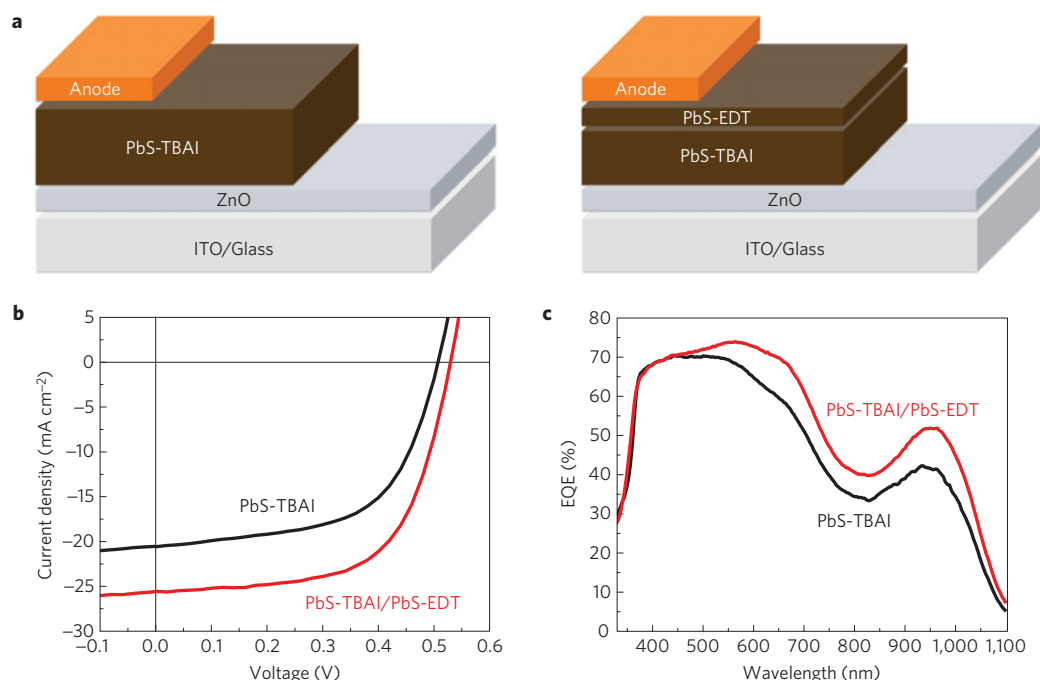
that employs layers of QDs treated with different ligands for different functions by tuning their relative band alignment—a layer of inorganic-ligand-passivated QDs serves as the main light-absorbing layer and a layer of organic-ligand-passivated QDs serves as an electron-blocking/hole-extraction layer. The devices show significant improvements in power conversion efficiency and long-term air stability, compared with previously reported devices.

Figure 1a shows the schematics of the device structures employed in this work. Oleic-acid-capped PbS QDs with the first exciton absorption peak at  $\lambda = 901$  nm in solution (Supplementary Fig. 1) are used to fabricate the thin films. Tetrabutylammonium iodide (TBAI) and 1,2-ethanedithiol (EDT) are used as the inorganic and organic ligands for solid-state ligand exchange. After solid-state ligand exchange, the first exciton absorption peak shifts to  $\lambda \sim 935$  nm, which corresponds to an optical bandgap  $E_g = 1.33$  eV. We find that PbS QD films treated with TBAI (PbS-TBAI) exhibit superior air stability compared with PbS QDs treated with EDT (PbS-EDT; Supplementary Fig. 2). PbS-TBAI-only devices also show a higher short-circuit current density ( $J_{SC}$ ), whereas PbS-EDT-only devices show a higher open circuit voltage ( $V_{OC}$ ; Supplementary Fig. 3).

The  $J$ - $V$  characteristics of photovoltaic devices with Au anodes are shown in Fig. 1b. The device consisting of 12 PbS-TBAI layers (corresponding to a film thickness of  $\sim 220$  nm) shows a power conversion efficiency of  $6.0 \pm 0.4\%$ , which is higher than the previously reported TiO<sub>2</sub>/PbS-TBAI devices consisting of PbS QDs with an additional solution phase CdCl<sub>2</sub> treatment and MoO<sub>3</sub>/Au/Ag anode<sup>4</sup>. Although PbS-EDT-only devices show a lower  $J_{SC}$  than PbS-TBAI-only devices, replacing the topmost two PbS-TBAI layers with two PbS-EDT layers significantly improves the  $J_{SC}$ ,  $V_{OC}$  and fill factor (FF), resulting in a  $\sim 35\%$  improvement in power conversion efficiency to  $8.2 \pm 0.6\%$ , with a 9.2% lab-champion device (Table 1).

We attribute the improvement in efficiency to the band offsets between the two PbS QD layers, which effectively block electron flow to the anode while facilitating hole extraction. We use ultraviolet photoelectron spectroscopy (UPS) to determine the band edge energies with respect to vacuum in PbS QD films (Fig. 2a). PbS-TBAI exhibits a deeper work function of 4.77 eV (that is,  $E_F = -4.77$  eV with respect to vacuum, where  $E_F$  is the Fermi level energy) than PbS-EDT. We attribute the difference in their work functions to the difference between the Pb-halide anion and the Pb-thiol-carbon interactions, which give rise to different surface dipole moments, as discussed elsewhere<sup>20</sup>. Furthermore, the difference between the

<sup>1</sup>Department of Materials Science and Engineering, Massachusetts Institute of Technology, Cambridge, Massachusetts 02139, USA, <sup>2</sup>Department of Physics, Massachusetts Institute of Technology, Cambridge, Massachusetts 02139, USA, <sup>3</sup>Department of Electrical Engineering and Computer Science, Massachusetts Institute of Technology, Cambridge, Massachusetts 02139, USA, <sup>4</sup>Department of Chemistry, Massachusetts Institute of Technology, Cambridge, Massachusetts 02139, USA. \*e-mail: [mgb@mit.edu](mailto:mgb@mit.edu)



**Figure 1 | Photovoltaic device architectures and performance.** **a**, Device architectures. **b**, Representative  $J$ - $V$  characteristics of devices with Au anodes under simulated AM1.5G irradiation ( $100 \text{ mW cm}^{-2}$ ). The PbS-TBAI device consists of 12 layers of PbS-TBAI and the PbS-TBAI/PbS-EDT device consists of 10 layers of PbS-TBAI and 2 layers of PbS-EDT. **c**, External quantum efficiency (EQE) spectra for the same devices.

**Table 1 | Solar cell performance parameters.**

|                             | $V_{oc}$ (V)              | $J_{sc}$ ( $\text{mA cm}^{-2}$ ) | FF (%)                | PCE (%)             |
|-----------------------------|---------------------------|----------------------------------|-----------------------|---------------------|
| PbS-TBAI*                   | $0.506 \pm 0.009$ (0.519) | $20.7 \pm 1.1$ (22.8)            | $57.7 \pm 1.9$ (59.6) | $6.0 \pm 0.4$ (7.0) |
| PbS-TBAI/PbS-EDT*           | $0.525 \pm 0.016$ (0.544) | $25.3 \pm 1.1$ (26.5)            | $61.6 \pm 1.3$ (63.8) | $8.2 \pm 0.6$ (9.2) |
| PbS-TBAI/PbS-EDT certified† | $0.5546 \pm 0.0055$       | $24.2 \pm 0.7$                   | $63.8 \pm 1.3$        | $8.55 \pm 0.18$     |

The numbers in parentheses represent the values obtained for the best-performing cell. \*To account for experimental errors, the reported averages and deviations are for samples of between six and nine devices on the same substrate from measurements performed between 1 and 75 days of air exposure. †Error bars: quoted uncertainties with an approximately 95% level of confidence.

Fermi level and valence band edge ( $E_V$ ) in PbS-TBAI is greater ( $E_F - E_V = 0.82 \text{ eV}$ ) than that in PbS-EDT ( $E_F - E_V = 0.63 \text{ eV}$ ). According to the individually determined band positions, the large conduction band offset (0.68 eV) between PbS-TBAI and PbS-EDT should block electron flow from the PbS-TBAI layer to the PbS-EDT layer. However, because the interactions between the PbS-TBAI and the PbS-EDT layers can affect the interfacial band bending, the actual band offsets in the device must be measured directly.

To determine the band alignment at the PbS-TBAI/PbS-EDT interface, we performed UPS measurements on PbS-TBAI films covered with different thicknesses of PbS-EDT (see Supplementary Information for the spectra and more details). As shown in Fig. 2a, as the thickness of the PbS-EDT layer increases, the Fermi level with respect to vacuum shifts to shallower energy levels and reaches saturation when the thickness of the PbS-EDT layer exceeds 13.5 nm. The shift indicates the formation of an interfacial dipole, which results in a reduction of the work function and a downward vacuum level shift at the interface. Moreover, the difference between the Fermi level and the valence band edge decreases with increasing PbS-EDT layer thickness. The energy level alignment at the PbS-TBAI/PbS-EDT interface deduced from the thickness-dependent UPS data is plotted in Fig. 2b.

The band alignment demonstrates the role of the PbS-EDT layer as an electron-blocking/hole-extraction layer between the PbS-TBAI layer and the anode, which leads to an improved photocurrent

collection efficiency and enhanced device performance in the PbS-TBAI/PbS-EDT devices. In the PbS-TBAI-only device, electron flow from PbS-TBAI to the anode, which is in the opposite direction to the photocurrent, and interfacial recombination at the PbS/anode interface are possible loss mechanisms (Fig. 2c). In the PbS-TBAI/PbS-EDT device, the conduction band offset between the PbS-TBAI and PbS-EDT layers provides an energy barrier that prevents photogenerated electrons (filled circles) from flowing to the PbS-EDT layer, whereas the valence band offset provides an additional driving force for the flow of photogenerated holes (open circles) to the PbS-EDT layer. The insertion of the PbS-EDT layer not only prevents electron flow from PbS-TBAI to the anode but may also reduce surface recombination of photogenerated electrons and holes at the PbS-TBAI/anode interface.

The interfacial band bending makes an additional minor contribution to the improved  $J_{sc}$ . The band bending at the PbS-TBAI/PbS-EDT interface implies the formation of a depletion region adjacent to this junction, which effectively extends the overall depletion width in the PbS-TBAI light-absorbing layer. This effect is similar to that in previously reported graded-doping devices<sup>15,16</sup> where control of carrier concentrations through ligand exchange extends the depletion region, although in that case the band edge positions of the PbS QDs were not altered<sup>16</sup>. The extension of the depletion region in those graded-doping devices accounts for a marginal increase (<5%) in  $J_{sc}$  compared with ungraded devices<sup>15,16</sup>.

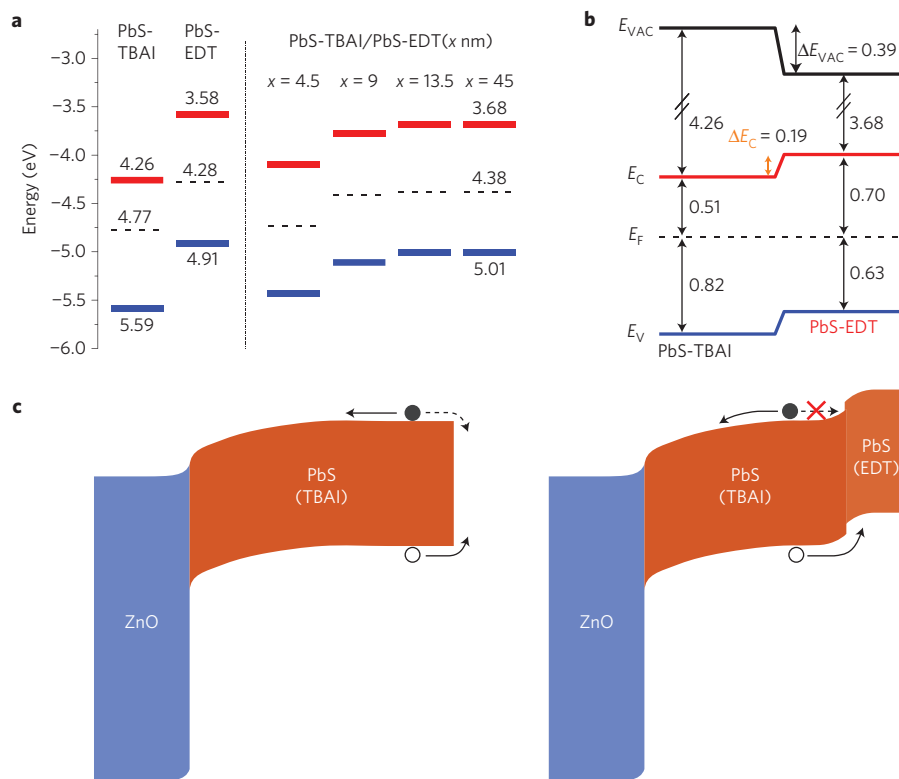


**Figure 2 | Energy level diagrams of PbS QDs and photovoltaic devices containing the QDs. a**, Energy levels with respect to vacuum for pure PbS-TBAI, pure PbS-EDT and PbS-TBAI films covered with different thicknesses of PbS-EDT layers. The Fermi levels ( $E_F$ , dashed line) and valence band edges ( $E_V$ , blue lines) were determined by UPS. The conduction band edges ( $E_C$ , red lines) were calculated by adding the optical bandgap energy of 1.33 eV, as determined from the first exciton absorption peak in the QD thin films, to  $E_V$ . **b**, Schematic energy level alignment at PbS-TBAI and PbS-EDT interfaces deduced from UPS, where  $E_{VAC}$  is the vacuum energy. **c**, Schematic illustration of proposed band bending in ZnO/PbS-TBAI (left) and ZnO/PbS-TBAI/PbS-EDT (right) devices at short-circuit conditions.

In our study, the PbS-TBAI/PbS-EDT devices typically show  $\sim 20\%$  improvements in  $J_{SC}$  compared with PbS-TBAI-only devices (Supplementary Fig. 14). As shown in Fig. 1c, the PbS-TBAI/PbS-EDT device exhibits a higher external quantum efficiency (EQE) than that in the PbS-TBAI-only device at longer wavelengths. Long-wavelength photons have longer penetration depths owing to the smaller absorption coefficients. Therefore, a higher fraction of long-wavelength photons are absorbed deeper in the film relative to the short-wavelength photons whose absorption is predominantly close to the ZnO/PbS-TBAI interface (Supplementary Fig. 16). The improvement in EQE at longer wavelengths clearly indicates a better photocurrent collection efficiency, especially in the region close to the PbS-TBAI/PbS-EDT interface, consistent with the proposed mechanisms. The  $J_{SC}$  values calculated by integrating the EQE spectra with the AM1.5G solar spectrum for PbS-TBAI-only and PbS-TBAI/PbS-EDT devices are  $21.0$  and  $23.7$   $\text{mA cm}^{-2}$ , respectively, which show good agreement with the measured  $J_{SC}$  ( $20.7 \pm 1.1$  and  $25.3 \pm 1.1$   $\text{mA cm}^{-2}$ ).

The device stability is found to depend to a greater extent on the interface and band alignment between the QDs and anodes than on the bulk QD layer itself. Figure 3 compares the evolution of solar cell performance parameters with air storage time in devices with Au and  $\text{MoO}_3/\text{Au}$  anodes, where the  $\text{MoO}_3$  is the commonly used hole-extraction layer in PbS-based and other organic photovoltaic devices<sup>21–24</sup>. Both PbS-TBAI and PbS-TBAI/PbS-EDT devices with Au anodes show stable performance compared with their counterparts with  $\text{MoO}_3/\text{Au}$  anodes. In contrast, devices with  $\text{MoO}_3/\text{Au}$  anodes developed S-shape  $J$ - $V$  characteristics after air exposure (Supplementary Fig. 8), consistent with the development of a Schottky barrier at the anode<sup>23–25</sup>. This

effect significantly reduces the FF and device performance, limiting air stability.

The mechanism through which  $\text{MoO}_3$  acts as the hole-extraction layer is through electron transfer from its deep-lying conduction band or from gap states to the active layer<sup>22–24</sup>. However, the positions of these states depend strongly on the stoichiometry, environment, and deposition conditions of the  $\text{MoO}_3$  (refs 22,26). It has been shown that briefly exposing a  $\text{MoO}_3$  film deposited under vacuum to oxygen can decrease its work function by more than 1 eV (ref. 27). Exposing  $\text{MoO}_3$  to humid air can decrease its work function even further<sup>28</sup>. The S-shaped  $J$ - $V$  characteristics in devices with a  $\text{MoO}_3$  anode are most likely due to unfavourable band alignment between PbS and air-exposed  $\text{MoO}_3$ . We note that the air-exposure time in which this effect becomes significant varies from batch to batch of fabricated devices as a result of uncontrolled humidity in ambient storage conditions. In contrast, the performance of devices without a  $\text{MoO}_3$  interfacial layer remains unchanged, implying that the PbS-TBAI absorber layers are functionally insensitive to oxygen and moisture during storage.

We also note that devices generally show an initial increase in  $V_{OC}$  and FF after air exposure regardless of the active layer (PbS-TBAI, PbS-EDT, or PbS-TBAI/PbS-EDT) and anode materials ( $\text{MoO}_3/\text{Al}$ ,  $\text{MoO}_3/\text{Au}$ , or Au). The ZnO/PbS films are fabricated and stored in air overnight before being transferred to a glovebox for anode deposition. The performance increases during the first hour of air exposure after evaporation of the metal electrodes (Supplementary Fig. 9). Therefore, further oxidation of the PbS QDs is unlikely to explain the performance enhancement. The origin of this initial increase in performance as a result of short air exposure is still under investigation.

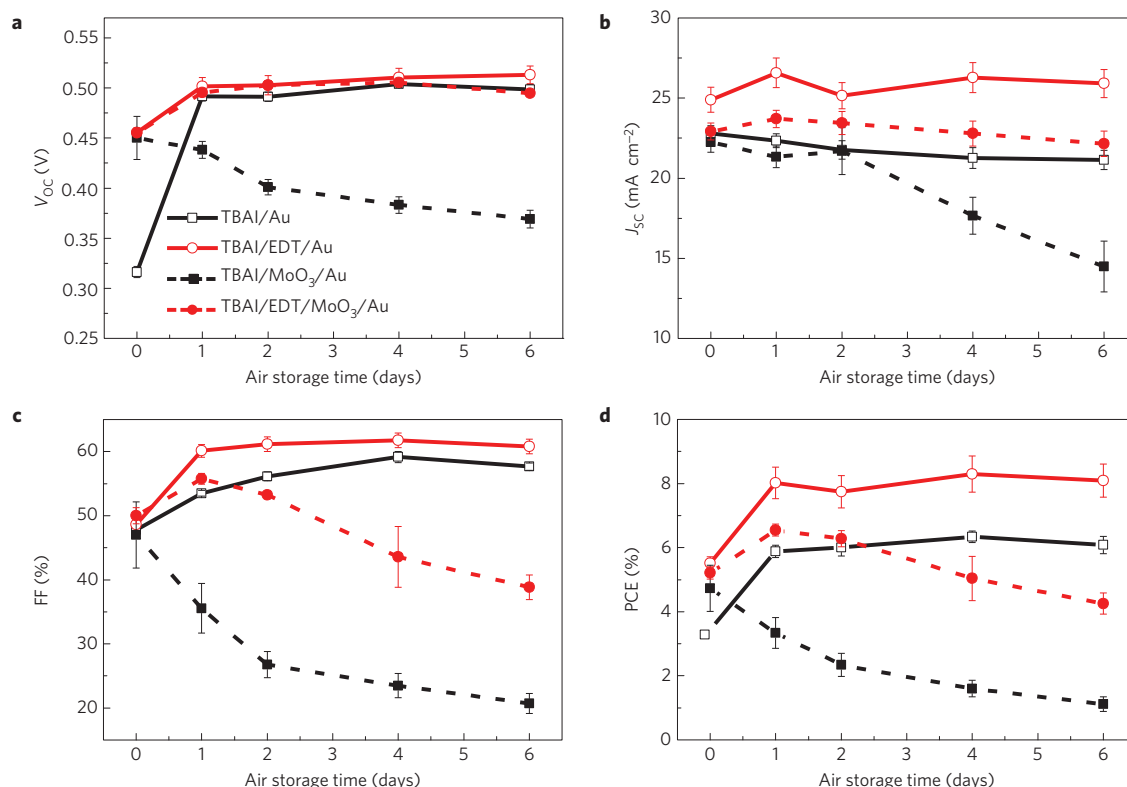


**Figure 3 | Evolution of photovoltaic parameters with air storage time in devices with Au and MoO<sub>3</sub>/Au anodes. a**, Open circuit voltage ( $V_{OC}$ ). **b**, Short-circuit current ( $J_{SC}$ ). **c**, Fill factor (FF). **d**, Power conversion efficiency (PCE). Measurements were performed in a nitrogen-filled glovebox. Day 0 denotes measurements performed after anode evaporation in vacuum. Between each measurement, the unencapsulated devices were stored in air without any humidity control. The average (symbols) and standard deviation (error bars) were calculated from a sample of six to nine devices on the same substrate.

The devices with Au anodes exhibit excellent long-term storage stability in air for over 150 days without any encapsulation (Fig. 4a). During the course of the stability assessment, devices are stored in air in the dark without humidity control but with some exposure to ambient light during sample transfer to the glovebox for testing. Devices have also been tested in air (Supplementary Fig. 10) and show no degradation in performance after testing. An unencapsulated device was sent to an accredited laboratory (Newport) after 37 days of air storage. This device, tested in air under standard AM1.5G conditions, shows a power conversion efficiency of  $8.55 \pm 0.18\%$  (Fig. 4b and Supplementary Fig. 10), which represents the highest certified efficiency to date for colloidal QD photovoltaic devices. To the best of our knowledge, it is also the highest certified efficiency to date for any room-temperature solution-processed solar cell. Another device certified after 131 days of air storage shows a comparable efficiency of  $8.19 \pm 0.17\%$  and the highest FF (66.7%) in QD solar cells to date (Supplementary Fig. 13).

In summary, we have demonstrated high-performance quantum dot solar cells through the engineering of band alignment at the QD/QD and QD/anode interfaces. These solar cells are processed in air at room temperature and exhibit excellent air-storage stability. Our results indicate that using inorganic-ligand-passivated QDs as the light-absorbing layer and removing the MoO<sub>3</sub> interfacial layer are essential to achieving air stability. Compared with other solution-processed solar cells, the present limiting factor of our device is the relatively low  $V_{OC}$ , where  $qV_{OC}$  ( $q$  is the elementary charge) is less than half of the optical bandgap. We expect that elucidating the origin of the low  $V_{OC}$ , optimizing combinations of ligands and QD sizes, and further improving surface passivation via solution-phase treatments will result in continued efficiency improvements. The simplicity of the room-temperature fabrication

process and the robustness of the devices to ambient conditions provide advantages compared with other solution-processed solar cells. Greater understanding of the QD optoelectronic properties and further progress in materials development could lead to a generation of air-stable, solution-processable QD-based solar cells.

## Methods

**Synthesis of colloidal PbS QDs.** The synthesis of oleic-acid-capped PbS QD with a first absorption peak at  $\lambda = 901$  nm was adapted from the literature<sup>11,29</sup>. Lead acetate (11.38 g) was dissolved in 21 ml of oleic acid and 300 ml of 1-octadecene at 100 °C. The solution was degassed overnight and then heated to 150 °C under nitrogen. The sulphur precursor was prepared separately by mixing 3.15 ml of hexamethyldisilathiane and 150 ml of 1-octadecene. The reaction was initiated by rapid injection of the sulphur precursor into the lead precursor solution. After synthesis, the solution was transferred into a nitrogen-filled glovebox. QDs were purified by adding a mixture of methanol and butanol, followed by centrifugation. The extracted QDs were re-dispersed in hexane and stored in the glovebox. For device fabrication, PbS QDs were further precipitated twice with a mixture of butanol/ethanol and acetone, respectively, and then re-dispersed in octane (50 mg ml<sup>-1</sup>).

**Synthesis of ZnO nanoparticles.** ZnO nanoparticles were synthesized according to the literature<sup>30</sup>. Zinc acetate dihydrate (2.95 g) was dissolved in 125 ml of methanol at 60 °C. Potassium hydroxide (1.48 g) was dissolved in 65 ml of methanol. The potassium hydroxide solution was slowly added to the zinc acetate solution and the solution was kept stirring at 60 °C for 2.5 h. ZnO nanocrystals were extracted by centrifugation and then washed twice by methanol followed by centrifugation. Finally, 10 ml of chloroform was added to the precipitates and the solution was filtered with a 0.45  $\mu$ m filter.

**Device fabrication.** Patterned ITO substrates (Thin Film Device Inc.) were cleaned with solvents and then treated with oxygen plasma. ZnO layers (120 nm) were fabricated by spin-coating a solution of ZnO nanoparticles onto ITO substrates. PbS QD layers were fabricated by layer-by-layer spin-coating. For each layer,  $\sim 10$   $\mu$ l of PbS solution was spin-cast onto the substrate at 2,500 rpm for



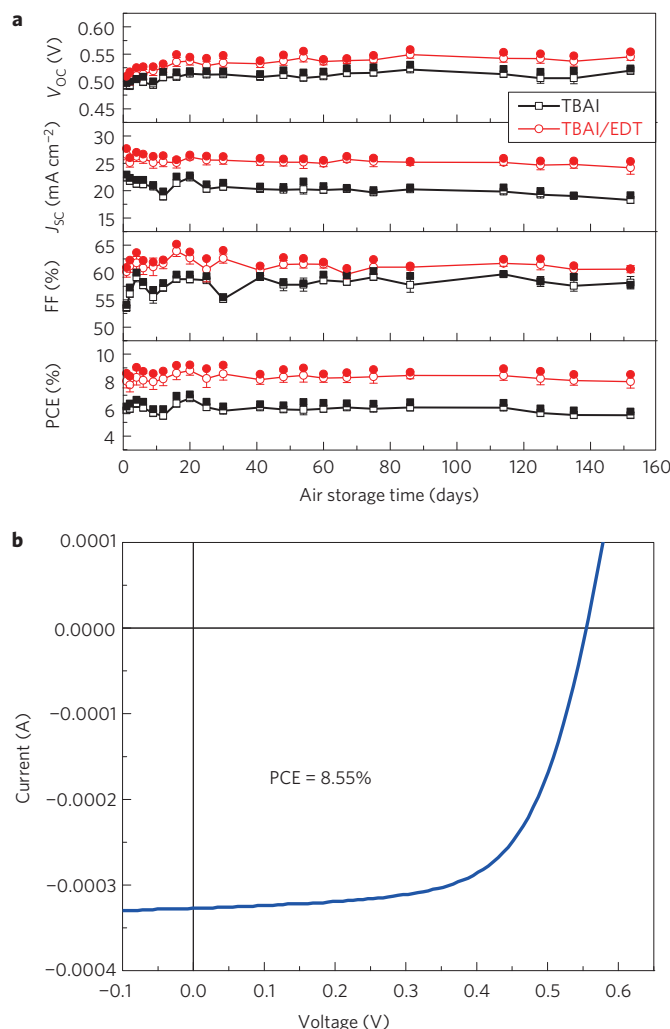


**Figure 4 | Long-term stability assessment of unencapsulated devices with Au anodes.** **a**, Evolution of photovoltaic parameters of PbS-TBAI (black) and PbS-TBAI/PbS-EDT (red) devices. Open symbols represent the average values and solid symbols represent the values for the best-performing device. **b**, Device performance of a PbS-TBAI/PbS-EDT device certified by an accredited laboratory (Newport) after 37 days of air storage.

15 s. A TBAI solution ( $10 \text{ mg ml}^{-1}$  in methanol) was then applied to the substrate for 30 s, followed by three rinse-spin steps with methanol. For PbS-EDT layers, an EDT solution (0.02 vol% in acetonitrile) and acetonitrile were used. All the spin-coating steps were performed under ambient condition and room light at room temperature. The thicknesses of each PbS-TBAI and PbS-EDT layer are about 18 nm and 23 nm, respectively, as determined by a profilometer (Veeco Dektak 6M). The films were stored in air overnight and then transferred to a nitrogen-filled glovebox for electrode evaporation.  $\text{MoO}_3$  (Alfa; 25 nm thick), Al or Au electrodes (100 nm thick) were thermally evaporated onto the films through shadow masks at a base pressure of  $10^{-6}$  mbar. The nominal device areas are defined by the overlap of the anode and cathode to be  $1.24 \text{ mm}^2$ . Larger-area devices ( $5.44 \text{ mm}^2$ ) have also been fabricated and show similar performance (Supplementary Figs 12 and 13). For certification of the larger area device, a  $3 \text{ mm}^2$  mask was attached to the device to define the device area.

**Device characterization.** Current–voltage characteristics were recorded using a Keithley 2636A sourcemeter under simulated solar light illumination (1-Sun,  $100 \text{ mW cm}^{-2}$ ) generated by a Newport 96000 solar simulator equipped with an AM1.5G filter. The light intensity was calibrated with a Newport 91150 V reference cell before each measurement. The error in efficiency measurements is estimated to be below 7%. EQE measurements were conducted under chopped monochromatic light from an optical fibre in an underfilled geometry without bias illumination. The light source was provided by coupling the white light from

a xenon lamp (Thermo Oriel 66921) through a monochromator into the optical fibre and the photocurrent was recorded using a lock-in amplifier (Stanford Research System SR830). Both current–voltage and EQE measurements were performed under an inert atmosphere unless stated otherwise. Devices were stored in ambient air between each measurement.

**Ultraviolet photoelectron spectroscopy.** PbS-TBAI and PbS-EDT samples for UPS measurements were fabricated in air using six layer-by-layer spin-coating steps to obtain  $\sim 110 \text{ nm}$ -thick PbS films on glass/Cr(10 nm)/Au(80 nm) substrates. For PbS-EDT-thickness-dependent UPS, a diluted PbS solution ( $10 \text{ mg ml}^{-1}$ ) was used to obtain the thinner PbS-EDT layers on PbS-TBAI films. The samples were then stored in air overnight before UPS measurements. UPS measurements were performed in an ultrahigh vacuum chamber ( $10^{-10}$  mbar) with a He(I) (21.2 eV) discharge lamp and have a resolution of 0.1 eV. Carbon tape was used to make electrical contact between the Cr/Au anode and the sample plate. A  $-5.0 \text{ V}$  bias was applied to the sample to enable accurate determination of the low-kinetic-energy photoelectron cut-off. Photoelectrons were collected at  $0^\circ$  from substrate normal and the spectra were recorded using an electron spectrometer (Omicron). The conduction band edge energies were calculated by adding the optical bandgap energy of 1.33 eV determined from the first exciton absorption peak in the QD thin films to the valence band edge energies. The  $E_F - E_V$  values have an error bar of  $\pm 0.02 \text{ eV}$  resulting from curve fitting.

Received 6 December 2013; accepted 15 April 2014;  
published online 25 May 2014

## References

- Graetzel, M., Janssen, R. A. J., Mitzi, D. B. & Sargent, E. H. Materials interface engineering for solution-processed photovoltaics. *Nature* **488**, 304–312 (2012).
- Wadia, C., Alivisatos, A. P. & Kammen, D. M. Materials availability expands the opportunity for large-scale photovoltaics deployment. *Environ. Sci. Technol.* **43**, 2072–2077 (2009).
- Zarghami, M. H. *et al.* p-Type PbSe and PbS quantum dot solids prepared with short-chain acids and diacids. *ACS Nano* **4**, 2475–2485 (2010).
- Tang, J. *et al.* Colloidal-quantum-dot photovoltaics using atomic-ligand passivation. *Nature Mater.* **10**, 765–771 (2011).
- Ip, A. H. *et al.* Hybrid passivated colloidal quantum dot solids. *Nature Nanotech.* **7**, 577–582 (2012).
- Choi, J. J. *et al.* Photogenerated exciton dissociation in highly coupled lead salt nanocrystal assemblies. *Nano Lett.* **10**, 1805–1811 (2010).
- Semonin, O. E. *et al.* Peak external photocurrent quantum efficiency exceeding 100% via MEG in a quantum dot solar cell. *Science* **334**, 1530–1533 (2011).
- Johnston, K. W. *et al.* Schottky-quantum dot photovoltaics for efficient infrared power conversion. *Appl. Phys. Lett.* **92**, 151115 (2008).
- Pattantyus-Abraham, A. G. *et al.* Depleted-heterojunction colloidal quantum dot solar cells. *ACS Nano* **4**, 3374–3380 (2010).
- Luther, J. M. *et al.* Stability assessment on a 3% bilayer PbS/ZnO quantum dot heterojunction solar cell. *Adv. Mater.* **22**, 3704–3707 (2010).
- Zhao, N. *et al.* Colloidal PbS quantum dot solar cells with high fill factor. *ACS Nano* **4**, 3743–3752 (2010).
- Tang, J. *et al.* Quantum junction solar cells. *Nano Lett.* **12**, 4889–4894 (2012).
- Rath, A. K. *et al.* Solution-processed inorganic bulk nano-heterojunctions and their application to solar cells. *Nature Photon.* **6**, 529–534 (2012).
- Chang, L.-Y., Lunt, R. R., Brown, P. R., Bulović, V. & Bawendi, M. G. Low-temperature solution-processed solar cells based on PbS colloidal quantum dot/CdS heterojunctions. *Nano Lett.* **13**, 994–999 (2013).
- Ning, Z. *et al.* Graded doping for enhanced colloidal quantum dot photovoltaics. *Adv. Mater.* **25**, 1719–1723 (2013).
- Yuan, M. *et al.* Doping control via molecularly engineered surface ligand coordination. *Adv. Mater.* **25**, 5586–5592 (2013).
- Jean, J. *et al.* ZnO nanowire arrays for enhanced photocurrent in PbS quantum dot solar cells. *Adv. Mater.* **25**, 2790–2796 (2013).
- Soreni-Harari, M. *et al.* Tuning energetic levels in nanocrystal quantum dots through surface manipulations. *Nano Lett.* **8**, 678–684 (2008).
- Jasieniak, J., Califano, M. & Watkins, S. E. Size-dependent valence and conduction band-edge energies of semiconductor nanocrystals. *ACS Nano* **5**, 5888–5902 (2011).
- Brown, P. R. *et al.* Energy level modification in lead sulfide quantum dot thin films through ligand exchange. *ACS Nano* <http://pubs.acs.org/doi/abs/10.1021/nn500897c> (2014).
- Shrotriya, V., Li, G., Yao, Y., Chu, C.-W. & Yang, Y. Transition metal oxides as the buffer layer for polymer photovoltaic cells. *Appl. Phys. Lett.* **88**, 073508 (2006).
- Meyer, J. *et al.* Transition metal oxides for organic electronics: Energetics, device physics and applications. *Adv. Mater.* **24**, 5408–5427 (2012).
- Gao, J. *et al.* n-type transition metal oxide as a hole extraction layer in PbS quantum dot solar cells. *Nano Lett.* **11**, 3263–3266 (2011).

24. Brown, P. R. *et al.* Improved current extraction from ZnO/PbS quantum dot heterojunction photovoltaics using a MoO<sub>3</sub> interfacial layer. *Nano Lett.* **11**, 2955–2961 (2011).
25. Gao, J. *et al.* Quantum dot size dependent *J–V* characteristics in heterojunction ZnO/PbS quantum dot solar cells. *Nano Lett.* **11**, 1002–1008 (2011).
26. Greiner, M. T. *et al.* Universal energy-level alignment of molecules on metal oxides. *Nature Mater.* **11**, 76–81 (2012).
27. Meyer, J., Shu, A., Kröger, M. & Kahn, A. Effect of contamination on the electronic structure and hole-injection properties of MoO<sub>3</sub>/organic semiconductor interfaces. *Appl. Phys. Lett.* **96**, 133308 (2010).
28. Irfan *et al.* Energy level evolution of air and oxygen exposed molybdenum trioxide films. *Appl. Phys. Lett.* **96**, 243307 (2010).
29. Hines, M. A. & Scholes, G. D. Colloidal PbS nanocrystals with size-tunable near-infrared emission: Observation of post-synthesis self-narrowing of the particle size distribution. *Adv. Mater.* **15**, 1844–1849 (2003).
30. Beek, W. J. E., Wienk, M. M., Kemerink, M., Yang, X. & Janssen, R. A. J. Hybrid zinc oxide conjugated polymer bulk heterojunction solar cells. *J. Phys. Chem. B* **109**, 9505–9516 (2005).

## Acknowledgements

The authors thank R. Brandt for help with the *J–V* measurements in air, T. Buonassisi for the use of the solar simulator in air, M. Baldo for the use of the UPS system,

and J. Jean for help with refractive index measurements. C-H.M.C thanks L-Y. Chang, D. Wanger, D-K. Ko, A. Maurano, I. Coropceanu and C. Chuang for fruitful discussions and technical assistance. P.R.B. was supported by the Fannie and John Hertz Foundation and the National Science Foundation. This work was supported by Samsung Advanced Institute of Technology. Part of this work made use of the MRSEC Shared Experimental Facilities at the MIT Center for Materials Science and Engineering (CMSE), supported by the National Science Foundation under award number DMR-08-19762, and the MIT Laser Biomedical Research Center (LBRC) under contract number 9-P41-EB015871-26A1, supported by the National Institute of Health.

## Author contributions

C-H.M.C and M.G.B. conceived and designed the project. C-H.M.C. performed most of the experiments and data analysis with some technical assistance from P.R.B. P.R.B. and C-H.M.C. performed UPS measurements and carried out their analysis. All authors discussed the results. C-H.M.C. wrote the manuscript with contributions from all authors.

## Additional information

Supplementary information is available in the [online version of the paper](#). Reprints and permissions information is available online at [www.nature.com/reprints](http://www.nature.com/reprints). Correspondence and requests for materials should be addressed to M.G.B.

## Competing financial interests

The authors declare no competing financial interests.